Superconductor
Science and
Technology

PAPER • **OPEN ACCESS**

Magnetic field–dependent vortex dynamics and critical currents in superconducting microwires with regular large-area perforation by pinholes

To cite this article: Dong Zhu *et al* 2025 *Supercond. Sci. Technol.* **38** 115010

OPEN ACCESS
IOP Publishing
Superconductor Science and Technology
Supercond. Sci. Technol. **38** (2025) 115010 (9pp)
https://doi.org/10.1088/1361-6668/ae1893

Magnetic field–dependent vortex dynamics and critical currents in superconducting microwires with regular large-area perforation by pinholes

Dong Zhu[1], **Ilya Charaev**[1], **Konstantin Ilin**[2] **and Andreas Schilling**[1,*]

[1] Department of Physics, University of Zurich, Winterthurerstrasse 190, CH-8057 Zurich, Switzerland
[2] Institute of Photonics and Quantum Electronics, Karlsruhe Institute of Technology (KIT), Karlsruhe 76131, Germany

E-mail: schilling@physik.uzh.ch

Received 8 April 2025, revised 6 August 2025
Accepted for publication 28 October 2025
Published 19 November 2025

Abstract

We report on the findings of simulations and experiments of vortex states in superconducting microwires with periodic rectangular pinhole structures. The simulations are performed by means of numerically solving the time-dependent Ginzburg–Landau (TDGL) equations. With increasing bias current and for different values of the external magnetic field applied normal to the structure plane, we first observe a vortex-free Meissner state, followed by a resistive vortex-flow mixed state and a state with a more intricate vortex pattern. The resulting dependence of the critical current I_c on magnetic field exhibits two plateaus with distinctly different vortex dynamics. Corresponding experimentally measured magnetic field dependences of I_c of WSi microwires with periodic pinhole structures and varying hole spacing confirm the predictions of these simulations, showing two ranges of magnetic field with almost field-independent critical currents. The experimentally determined critical currents are larger for smaller pinhole spacings, in agreement with the results of TDGL simulations. The good agreement of the simulations with the experimental observations presents a convenient strategy for the optimization of single-photon detectors with or without artificial and natural defects.

Supplementary material for this article is available online

Keywords: Ginzburg–Landau equations, superconducting films, vortex dynamics, pinholes, critical current

---

[*] Author to whom any correspondence should be addressed.

1. Introduction

Superconducting micrometer-wide single-photon detectors (SMSPDs), which can be fabricated from a variety of materials such as NbN, MoSi, WSi, and NbRe, have recently garnered significant attention [1–7]. The extension of nanowires to micrometer-wide wires and the corresponding expected alteration of the light detection mechanism at work offer numerous avenues for further exploration. For SMSPDs, the mechanism of light-quanta detection is likely based on vortex generation and motion. The energy released by normal-state electrons accompanying the vortex motion generates a voltage pulse that can be detected by an external circuit. Therefore, the vortex dynamics in microwires is a particularly important and valuable subject for investigation [1, 8, 9]. Recently, it has been experimentally shown [5] that dark counts of such detectors in a magnetic field can be suppressed effectively by perforating the microwires with a grid of pinholes; moreover, the magnetic field dependence of the critical current shows a peculiar plateau at low magnetic fields around zero. Therefore, artificially perforated pinhole structures or random defects created by energetic ion bombardment can drastically affect the photon-detection performance in superconducting micro- and nanowires [4, 10–12].

For superconducting thin films or micrometer and submicrometer wide strips without pinholes, single or multiple vortex motion has been investigated theoretically and computationally [9, 13, 14]. Vortex motion is directly causally related to the magnitude of the critical current as defined by the current-induced transition from the superconducting to a resistive state. In the case of a single defect (one hole or an area of suppressed superconductivity), a qualitative analysis already allows for a good description and prediction of the behavior of the system. As reported by Vodolazov *et al* [15], two mechanisms, namely, the vortex entry via the edge of the microstrip, and the creation of vortex–antivortex pairs nucleating in the vicinity of the hole, determine the critical current in such structures in the presence of an applied current and in an external magnetic field. In the case of many spatially distributed defects, a simple qualitative analysis of such complex systems is no longer possible; therefore, simulations on the basis of the time-dependent Ginzburg–Landau theory (TDGL) are required [16].

In this work, we computationally study the vortex dynamics in superconducting microwires with three columns of pinhole chains with varying pinhole distance in a rectangular periodic arrangement. TDGL simulations directly demonstrate the dynamics of the vortex state of the microwires in the presence of a bias current and an external magnetic field, with vortex-free Meissner states that are well distinguishable from resistive vortex flow states appearing with increasing current and show a remarkable complexity of the vortex arrangement at large bias currents. Using a suitable realistic voltage threshold, our simulations allow us to determine the critical current as a function of the magnetic field.

We find that the critical current in varying magnetic fields exhibits two distinct plateaus, regardless of the size of the pinhole spacing. The time-dependent vortex evolution near these two critical-current plateaus suggests that the presence of the pinholes enhances the vortex-free Meissner state in the first plateau and stabilizes the vortex-flow mixed state in the second plateau. To verify the findings of these simulations, we have experimentally examined WSi microwires with corresponding pinhole structures for three different longitudinal pinhole spacings and have observed the two predicted critical-current plateaus in an external magnetic field. By comparing the results for different pinhole spacings, we also find that smaller hole spacings correspond to higher critical currents, suggesting an influence on the vortex dynamics by the geometrical configuration of the pinholes and improving the current-carrying capability of the microwires.

2. Simulation details

In this work, TDGL simulations were primarily performed using the Python computational package pyTDGL presented in [17], which can solve vortex and phase dynamics in arbitrarily shaped 2D superconducting thin films, with an applied external magnetic field, bias current, or both. pyTDGL is based on the generalized time-dependent Ginzburg–Landau equation, which has the dimensionless form:

$$\frac{u}{\sqrt{1+\gamma^2|\psi|^2}}\left(\frac{\partial}{\partial t}+\mathrm{i}\varphi(\boldsymbol{r},t)+\frac{\gamma^2}{2}\frac{\partial|\psi|^2}{\partial t}\right)\psi(\boldsymbol{r},t)$$
$$=(\epsilon-|\psi|^2)\psi(\boldsymbol{r},t)+(\nabla-\mathrm{i}\boldsymbol{A}(\boldsymbol{r},t))^2\psi(\boldsymbol{r},t), \tag{1}$$

where $\psi(\boldsymbol{r},t)=|\psi|\,\mathrm{e}^{\mathrm{i}\theta}$ is the superconducting order parameter describing the superconducting condensate at position $\boldsymbol{r}$ and time t, and $\varphi(\boldsymbol{r},t)$ and $\boldsymbol{A}(\boldsymbol{r},t)$ are the Coulomb and the magnetic vector potentials in the superconducting film, respectively. The parameter ϵ is a real-valued number adjusting the local critical temperature of the film and is set here to 1 by default. The constant $u=\pi^4/14\zeta(3)\approx 5.79$ is the ratio of relaxation times to the amplitude and phase of the order parameter in dirty superconductors, and γ is a measure of the inelastic electron-phonon scattering strength, which is set to 1 in our simulations [8, 9, 17].

The potential fields associated with the normal current density satisfy the equation:

$$\nabla^2\varphi(\boldsymbol{r},t)=\nabla\cdot\boldsymbol{J}_\mathrm{s}=\nabla\cdot\mathrm{Im}\,\psi^*(\nabla-\mathrm{i}\boldsymbol{A}(\boldsymbol{r},t))\psi(\boldsymbol{r},t) \tag{2}$$

where $\boldsymbol{J}_\mathrm{s}$ is the supercurrent density, accounting for the fact that the total current in the film is free from divergence. Together with appropriate boundary conditions, pyTDGL employs a finite element analysis to solve the time dependence of the order parameter, the supercurrent density, the normal current density, the Coulomb potential and the magnetic field distribution in superconducting thin films.

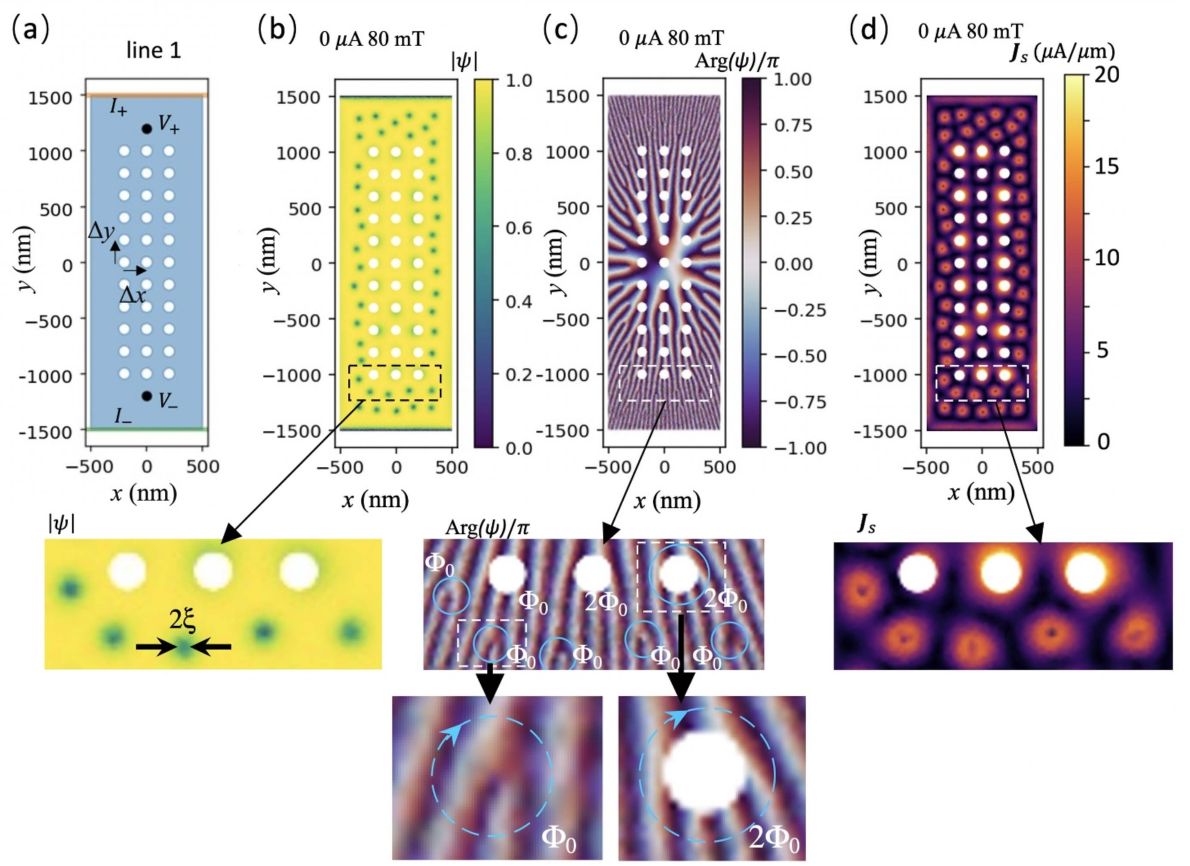

Figure 1. (a) Design of the superconducting microline 1 perforated with pinholes, with a transverse width $w = 1$ μm and length $L = 3$ μm. The pinholes with diameter $D = 100$ nm are arranged in a rectangular arrangement, for line 1 at equal distances $\Delta x = 200$ nm in the transverse and $\Delta y = 200$ nm in the longitudinal direction, respectively; (b)–(d) the mixed state of microline 1 as an example, in an applied magnetic field of 80 mT and without bias current. The figures, from left to right, show (b) the amplitude $|\psi|$ of order parameter, (c) its phase, and (d) the corresponding supercurrent density J_s per unit width, with circular screening currents forming the vortices. A magnification of the dashed rectangular areas is shown below these figures, indicating the size $\approx 2\xi$ of a vortex core in the left panel. A further magnification of the phase map (bottom panels) illustrates the bifurcation phenomenon for a single vortex carrying one flux quantum Φ_0 (left bottom panel) and for a vortex with two flux quanta, trapped by a pinhole (right bottom panel), marked with blue dashed circles. The London magnetic penetration depth λ and the coherence length ξ for this simulation were selected as 960 nm, and 13.6 nm, respectively.

In these simulations, we canprobe the time evolution of the order parameter $\psi(\boldsymbol{r}, t)$ and directly observe the creation of magnetic vortices. Moreover, by setting voltage probing points as shown in figure 1(a), we can also obtain the evolution of the voltage over time due to vortex flow and define a critical current using a suitably selected voltage threshold. Based on the pyTDGL simulation package where the G–L equations are dimensionless [17], we can convert the corresponding dimensionless times and voltages to physical units by multiplying them with the characteristic time $\tau_0 = \mu_0 \sigma \lambda^2$ and voltage $V_0 = \frac{4\xi^2 B_{c2}}{\mu_0 \sigma \lambda^2} = \frac{2\Phi_0}{\pi \mu_0 \sigma \lambda^2}$, respectively, where λ is the magnetic penetration depth, ξ the coherence length, μ_0 the permeability of the vacuum, Φ_0 the magnetic flux quantum, and B_{c2} the upper-critical field. For a typical WSi microwire, the conductivity is $\sigma = \frac{1}{R_s d} = 5 \times 10^5$ S m^{-1}, whereas the normal sheet resistance R_s and the thickness d of the strip are set to $R_s = 1000$ Ω [5] and $d = 2$ nm, respectively, to account for the actual values in the subsequent experiments. The resulting characteristic time and voltage units are, with chosen $\lambda = 960$ nm (see supplementary material), $\tau_0 = 0.58$ ps, and $V_0 = 2.3$ mV, respectively.

3. Results

For our numerical calculations, we have initially modeled microline 1 (in the following abbreviated as "line1"), with length $L = 3$ μm and width $w = 1$ μm, see figure 1(a). It contains pinholes with hole diameter $D = 100$ nm, arranged in a rectangular configuration with equal hole spacings $\Delta x = \Delta y = 200$ nm in the transverse and longitudinal directions, respectively. In our calculations, we used parameters of a typical WSi microwire with a thickness of 2 nm, with a London penetration depth $\lambda = 960$ nm as obtained from the measured kinetic inductance in pulse-shape experiments on the devices as described in the supplementary material and varying coherence lengths of the order of $\xi \approx 13$ nm [5]. Figure 1(b) shows the resulting mixed state of this line in an external magnetic field of 80 mT and without bias

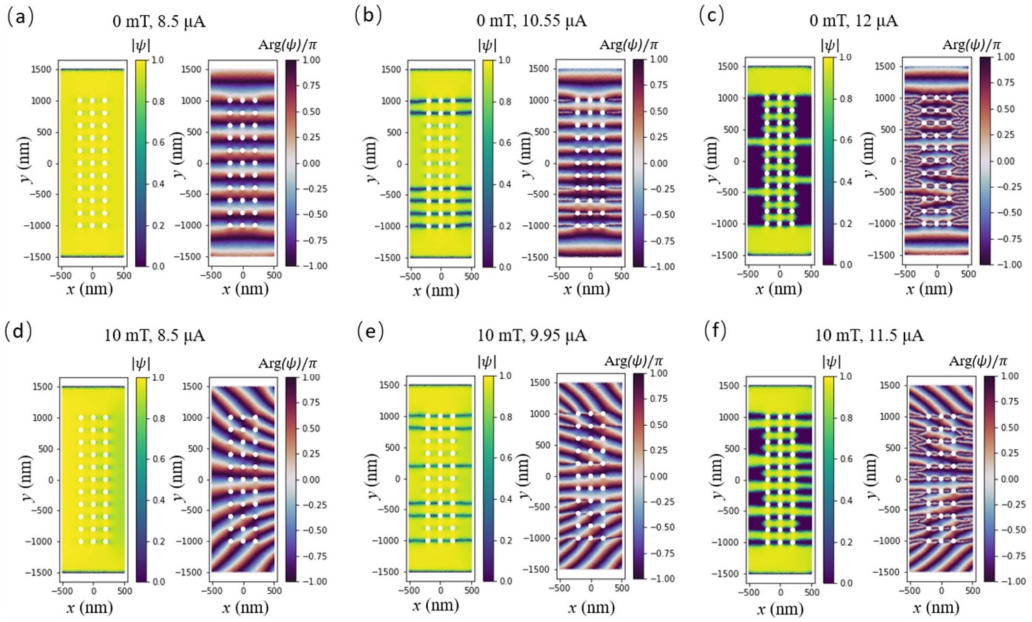

Figure 2. Amplitude $|\psi|$ and phase $\mathrm{Arg}(\psi)/\pi$ of line 1 at different bias currents as indicated on top of each pair of figures for two selected magnetic fields 0 mT (a)–(c) and 10 mT (d)–(f), with the bias current in the y-direction flowing from top to bottom, and the magnetic field directing out of the sample plane; (a), (d) vortex-free Meissner states; (b), (e) vortex-flow mixed states around the respective critical currents I_c, and (c), (f) above I_c in the resistive state, showing patchy normal-state regions in near the pinholes (see also the movies provided in the supplementary material for details and the possibility to zoom into the graphs).

current as an example. As expected [18], quantized vortices appear in the sample, with the order parameter amplitude $|\psi|$ gradually decreasing at the centers (green circles with approximate diameter 2ξ, see magnification in the lower left panel of figure 1). The phase of the order parameter $\mathrm{Arg}(\psi)$ is shown in figure 1(c). The unpinned vortices are primarily distributed at the edge of the sample, and the resulting superconducting screening currents (red rings) can be clearly observed in figure 1(d) [19]. The red color along the edges of the line represents the Meissner shielding current. The overall phase pattern shows a divergent distribution from the center outward, with a slight asymmetry due to nonuniform magnetization as a consequence of the nonuniform vortex distribution. Unlike for freely moving vortices, the phase changes around certain pinholes are 4π (corresponding to two magnetic flux quanta, $2\Phi_0$), such as for the top left and the bottom right two pinholes, among others, whereas the majority show a phase change of 2π as expected, carrying one magnetic flux quantum Φ_0. These phase changes manifest themselves in the corresponding bifurcations in the phase map as displayed in the corresponding magnifications of figure 1(c) (lower panels).

Figure 2 shows the amplitudes and phases of the superconducting order parameter ψ in the superconducting state of line 1 at different bias currents and for two values of the external magnetic field of 0 and 10 mT. The same material parameters as in figure 1 ($\lambda = 960$ nm and $\xi = 13.6$ nm) were used for this simulation. With increasing current, the superconducting state appears to transform from a pure Meissner state to a state with a regular vortex flow distribution slightly below the respective critical currents I_c, and eventually to a resistive state at even larger currents. To determine these critical current values, we have selected a voltage-threshold criterion to be discussed in detail further below.

At zero magnetic field and below the critical current as shown in figure 2(a), the amplitude of the order parameter remains almost constant at 1, and the phase exhibits a plane-wave periodic variation reflecting the flow of the supercurrents. The absence of significant variations of the order parameter near the pinholes suggests that there is no vortex or vortex-pair generation at these sites. A slight suppression of the amplitude of the order parameter between the pinholes reflects weak current crowding. In $B = 10$ mT and below the respective critical current, figure 2(d), the amplitude of the order parameter is partly suppressed in the right half of the strip. The spatial variation of the phase along the y-axis shows a distinct gradient, which reflects the uneven distribution of the supercurrents, but the system remains in pure Meissner state as no vortices appear [20]. This situation can be described qualitatively in the following way. The suppression of the order parameter at the right edge of the strips is a consequence of the fact that the bias and Meissner currents are flowing in the same direction, thereby reducing the order parameter more than at the left edge where these current directions are opposite. A certain suppression of the order parameter is also observed between the middle and the right column of the pinholes and at the right side of the latter pinholes. Here, the local current density is increased due to current crowding.

In the state of vortex flow at currents near the respective critical values, as shown in figures 2(b) and (e), several continuous horizontal lines with strongly suppressed order parameter appear, connecting the pinholes. For example, in zero magnetic field, figure 2(b), the amplitude of the order

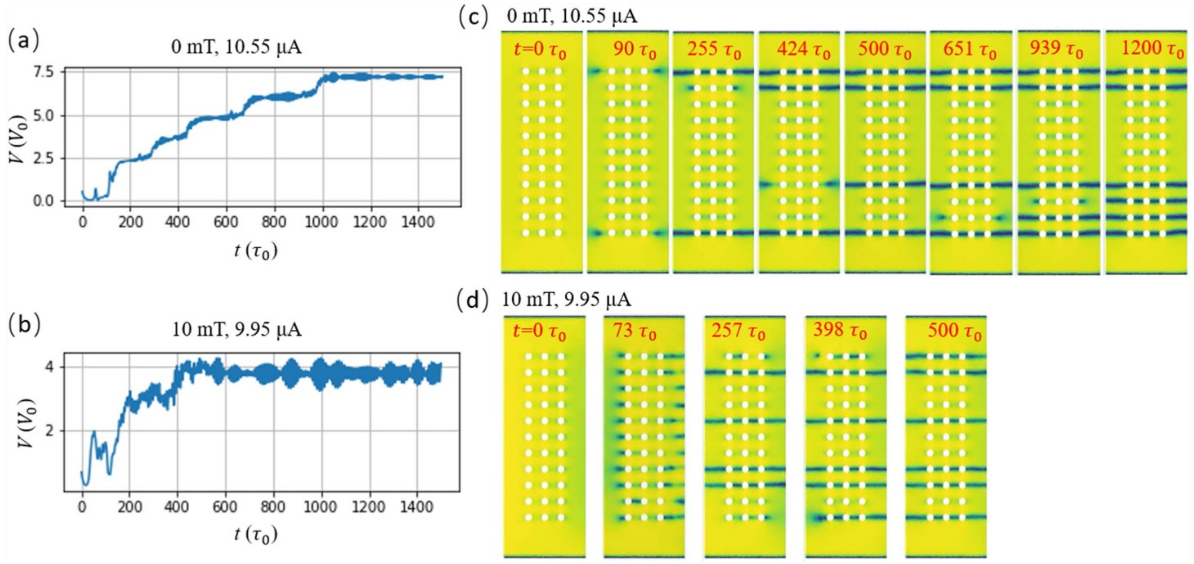

Figure 3. (a), (b) Evolution of the voltage across the line 1 over a 1500 $\tau_0 \approx 0.9$ ns time period for two sets of magnetic field and bias current around the respective critical current, assuming a coherence length $\xi = 13.6$ nm; (c) Time slices of the order parameter amplitude at 0 mT and 10.55 μA; (d) Corresponding data for 10 mT and 9.95 μA.

parameter is suppressed across the full width of the strip in six rows of pinholes. In the other regions, the spatial distribution of the order parameter remains virtually unchanged as compared to figure 2(a) [21, 22]. In a magnetic field of 10 mT, figure 2(e), the phase of the order parameter displays a clear bifurcation phenomenon at certain pinhole sites, which is a typical indication that vortex lines are trapped at these positions.

At even larger bias currents beyond the critical current, a vortex flow state appears that displays peculiar patterns, as shown in figures 2(c) and (f). The order parameter is suppressed in such a manner that patchy normal state regions form in proximity to the pinholes, resulting in a phase landscape that becomes exceedingly delicate and appears to be almost chaotic on both sides of the pinhole rows [9, 13].

We now turn to the details of the time evolution of the voltage across the bridge based on our simulations of line 1. After applying a bias current of 10.55 μA at $t = 0$ in zero magnetic field, vortex–antivortex pairs are created and move horizontally outward from the pinholes to the edges within certain pinhole rows, accompanied by a voltage increase from zero due to the dissipative vortex motion. The generated voltage turns out to be proportional to the number of such rows showing vortex flow, and it therefore exhibits a stepwise increase over time as depicted in figure 3(a). This outcome reflects the fact that the generation of vortices is discontinuous, and a transient saturation of the number of flowing vortices occurs at each voltage step. In the first step, the voltage rises by 2.5 voltage units, whereas the subsequent four steps correspond to 1.25 units, summing up to 7.5 units and 6 affected pinhole rows in the final state, as also shown in figure 2(b). The 1:1 correspondence between voltage and the number of pinhole rows exhibiting regular vortex flow can been clearly seen by inspecting the time sequence of the order parameter of line 1 in figure 3(c), and in the detailed movies provided in the supplementary material. The fact that vortices first appear at the top and the bottom of the microstrip is attributed to the current crowding at both ends where the uniform current meets the field of pinholes. The region of the vortex-free Meissner state is kept as large as possible throughout the whole process.

The corresponding evolution of the voltage over time in a magnetic field of 10 mT with a bias current of 9.55 μA is shown in figures 3(b) and (d), along with the accompanying variations of the order parameter and the creation of line structures connecting pinholes within individual rows. The system starts already with a weak current-crowding effect due to the presence of the Meissner current. In contrast to the zero-field case, the vortex flow is initially triggered in all pinhole rows immediately after turning on the bias current due to this current crowding, as is shown for $t = 73\ \tau_0$ in figure 3(d), and the voltage rapidly increases to 2 voltage units before partially decaying to a lower value. Afterward, as in the zero-field case, more and more pinhole rows exhibit continuous vortex flow with increasing duration of the process, until a final state is reached with a stable voltage. The fact that the voltage (and therefore resistance) steps in zero magnetic field and in 10 mT are not equal stems from the fact that the order parameter suppression within a pinhole row for the selected different bias currents turns out to be different at 10 mT than at zero field. We present a complete set of simulated *I*–*V* data in the supplementary material.

Since the dissipated power caused by vortex motion can drive a microwire from the superconducting to the normal state, a threshold voltage should be chosen to define the value of the critical current I_c and its variation in an external magnetic field that can eventually be compared with experimental results. We note, however, that the evolution of the voltage as shown in figure 3 and the *I*–*V* curves presented in the supplementary material correspond to a case where Joule heat has no direct effect on the behavior of the electronic system, i.e. a

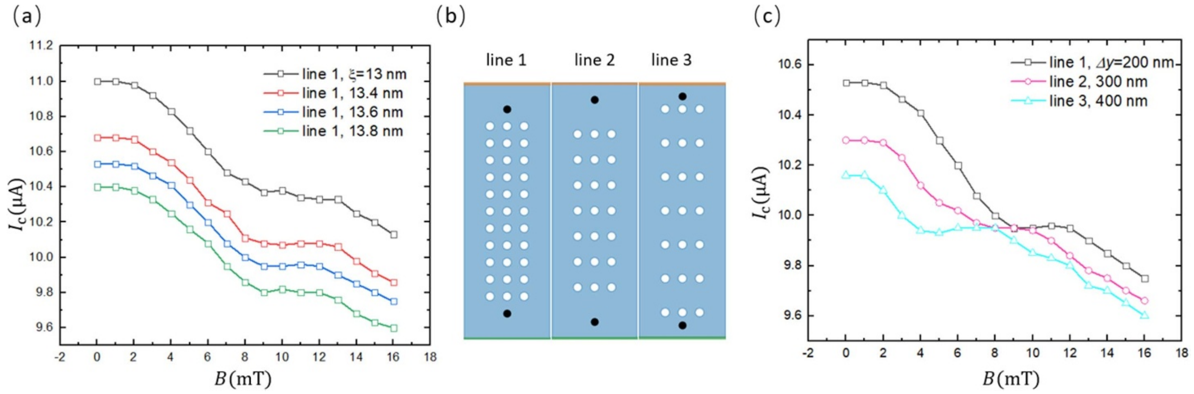

Figure 4. (a) Simulated critical current vs. magnetic field of line 1 for four superconducting coherence lengths, $\xi = 13$ nm (black), 13.4 nm (red), 13.6 nm (blue) and 13.8 nm (green); (b) hole arrangements for lines 1–3 with vertical distances $\Delta y = 200$ nm (line 1), 300 nm (line 2) and 400 nm (line 3) between the holes, with identical dimensions 3×1 μm^2 of the superconducting film and pinhole diameter $D = 100$ nm. (c) simulated critical current vs. magnetic field for three lines with fixed coherence length $\xi = 13.6$ nm and identical voltage threshold $4V_0$ ($\approx$9 mV).

situation with perfect thermal anchoring as it could be realized, for instance, by immersing the thin film in superfluid helium. In reality, the transition to the normal state can result in a local temperature increase within the film material that can ultimately lead to thermal latching (see supplementary material), so that the measured $V(t)$ and I–V curves would deviate from those obtained by the present simulations. Nevertheless, the bias current leading to a suitably chosen low threshold voltage should still reflect the technical critical current I_c that is measured in an actual experiment, above which possible thermal latching could occur.

We have chosen $4V_0$ ($\approx$9 mV) as a threshold voltage, which corresponds to a stable vortex flow across about half of the pinhole rows for line 1 in $B = 10$ mT. Figure 4(a) shows the dependence of the critical current $I_c(B)$ on the magnetic field as calculated for four different coherence lengths, $\xi = 13$ nm, 13.4 nm, 13.6 nm, and 13.8 nm, respectively. At zero magnetic field, the simulated $I_c(0)$ decreases with increasing coherence length, and corresponds to 11.0 μA, 10.68 μA, 10.53 μA, and 10.4 μA, respectively. In a weak magnetic field up to 1–2 mT, the critical currents remain almost constant, i.e. independent of the applied magnetic field. A further increase of B beyond 2 mT up to $\approx$9 mT results at first in a decrease of I_c, but it then becomes again comparably weakly dependent on magnetic field up to $B \approx 13$ mT, thereby forming a second plateau-like feature in $I_c(B)$. The I_c values at the second plateau also decrease with the increasing ξ, to 10.34 μA, 10.08 μA, 9.95 μA, and 9.8 μA, respectively. Beyond $B \approx 13$ mT, the I_c values decrease again upon further increasing the magnetic field. This double critical-current plateau effect in the magnetic-field dependence of I_c is significantly different from the previously reported behavior of the critical current of microwires with one hole or with a triangular hole pattern, where only a single current plateau around $B = 0$ was observed [5, 15]. We therefore conclude that microwires with different hole arrangements can react very differently in an external magnetic field.

We note here that the magnetic field values at the observed plateaus do not coincide with the vortex-matching field $B_m \approx 52$ mT, which we estimated from $B_m \approx \Phi_0/\Delta x^2$, assuming one magnetic flux quantum per hole and a geometric cell of area Δx^2. Although this fact may be counterintuitive, it suggests that other factors primarily determine the occurrence and width of the $I_c(B)$ plateaus. Such a plateau has also been observed in lines with a single hole [15], for which a matching field cannot be defined, and the width of the resulting plateau is clearly related to the diameter of the hole. It has been argued that, in bridges without holes, vortices form at the edges. In contrast, in the plateau region of the corresponding pinhole bridges, vortex-antivortex pairs are generated near the holes [15], which aligns with our observations (see figures 3(c) and (d) and the movies in the supplementary material).

To study the possible effect of the longitudinal hole spacing, we performed additional simulations for microwires with vertical hole distances $\Delta y = 300$ nm (line 2) and 400 nm (line 3), with the same transverse hole distance $\Delta x = 200$ nm and hole diameter $D = 100$ nm, patterned in bridges of identical size 3×1 μm^2. As a result, the number of rows decreases from 11 (line 1) to 7 (lines 2 and 3). Figure 4(c) shows the dependence of the critical current on the magnetic field obtained for these microwires by fixing the coherence length to $\xi = 13.6$ nm and using the same voltage threshold as for line 1. Two critical current plateaus in $I_c(B)$ also develop in the lines 2 and 3. The critical currents for the first plateau ($B = 0$) decrease systematically with increasing hole distance, from 10.53 μA to 10.3 μA and 10.16 μA, respectively. The I_c value at the second current plateau is approximately 9.95 μA, independent of Δy, which may be a coincidence. In contrast, the magnetic field range spanning the second plateau clearly and systematically shifts to smaller magnetic fields (from 9 to 12 mT in line 1 to 4–8 mT in line 3). As the number of pinhole rows is identical in lines 2 and 3, we may tentatively conclude that the observed tendency of an overall decrease of I_c and a shift of the second plateau to lower magnetic fields with increasing longitudinal

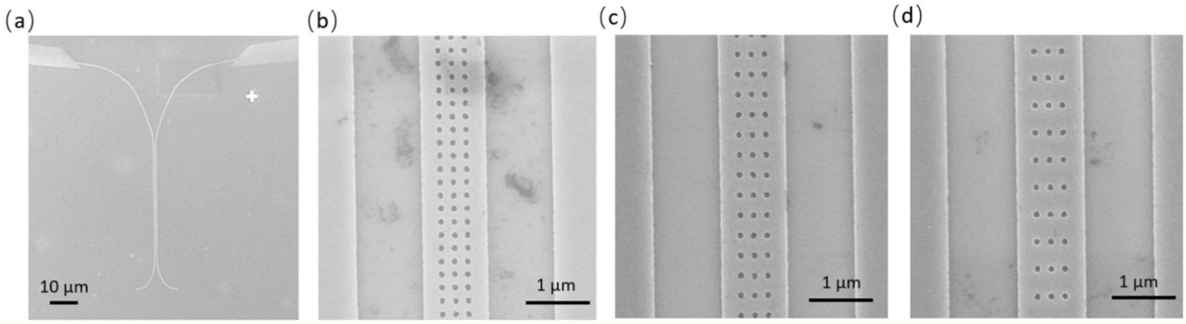

Figure 5. SEM images of the samples used in the experiments: (a) 1 μm wide and 90 μm long straight microwire with a pinhole grid; (b) enlarged view of exp-line 1, with pinhole diameter $D = 100$ nm, and transverse and longitudinal hole spacing $\Delta x = \Delta y = 200$ nm, respectively; (c) exp-line 2 with $\Delta y = 300$ nm; (d) exp-line 3 with $\Delta y = 400$ nm.

hole spacing is an intrinsic trend, which is likely caused by a systematic variation of the respective vortex dynamics with varying hole distance [23–28]. It is therefore conceivable that, in the hypothetical limit of an infinitely large Δy, corresponding to a single row of pinholes, only a single plateau remains around $B = 0$, as it has been observed in experiments with a single defect [15].

4. Experimental confirmation

In order to test the pyTDGL simulation results for superconducting microlines with pinholes with respect to the vortex dynamics, and in particular to the possible appearance of two critical current plateaus in a magnetic field, we performed experiments on dedicated WSi microwires. Figure 5 shows the SEM images of three structures made of a 2 nm-thick WSi film, with exact composition $W_{0.59}$ $Si_{0.41}$, sheet resistance of 1000 Ω sq^{-1}, and a critical temperature of 2.4 K [5]. The dimensions of the microwires were $w = 1$ μm and $L = 90$ μm (figure 5(a)). The pinhole arrangements and sizes in the experimentally investigated microlines (denoted in the following as exp-line 1, 2, and 3) are the same as the model lines in figures 1 and 4, with a transverse spacing $\Delta x = 200$ nm and vertical spacing $\Delta y = 200$ nm, 300 nm, and 400 nm, respectively, see figures 5(b)–(d). The measurements were conducted in a dilution refrigerator (Oxford Instruments Inc.) with a base temperature of 250 mK. The magnetic field was generated by a built-in commercial superconducting magnet and controlled by a Mercury iPS power system with an accuracy of 1 mT. To measure critical currents and detect voltage pulses, we used a commercially available single-photon probing platform with an integrated low-noise voltage bias and amplifier (PHOTEC), photon counter SR400, and DPO 7354 oscilloscope.

The magnetic field dependence of the critical currents $I_c(B)$ of all three lines with pinholes is displayed in figure 6(a). They all show a comparable behavior to the two plateaus of the critical current, see figure 6(b)). At the first plateau around zero magnetic field, the critical current values $I_c(0)$ are 10.65 μA, 10.25 μA, and 10.10 μA for the exp-lines 1–3, respectively. As predicted by the results of the simulations discussed above, we observe a second plateau in all three types of lines, with critical-current values 9.75 μA, 9.65 μA, and 9.25 μA, respectively. These experimental results not only clearly confirm the occurrence of two critical current plateaus for a rectangular pinhole pattern in superconducting bridges but also correctly reproduce the qualitative correlation between the value of the critical current and the longitudinal hole spacing as predicted by the pyTDGL numerical simulations. In figure 6(c), we tentatively directly compare the experimental and simulated $I_c(B)$ dependences from figure 4(a) for exp-line 1, with the best match for $\xi = 13.4$ nm and 13.6 nm.

However, we do not expect a perfect reproduction of all experimental data from our simulations. While the second plateaus are well developed in the experiments, they are all located between approximately 6 mT and 14 mT and do not show any clear shift with varying Δy as suggested by the simulated results shown in figure 4(c). Moreover, the measured magnetic field dependences of $I_c(B)$ within and beyond the second plateaus are stronger than predicted [20]. Possible reasons for these discrepancies are manifold. First, the lines studied in the experiments were considerably longer than those in the simulations for practical reasons. Additional influences may include inadequate modeling of the properties and geometry at the edges of the lines, the pinholes and the electrodes, and deviating material parameters. We also disregarded possible thermal latching processes in the simulation due to the difficulty of modeling all relevant heat flows (see supplementary material for more details), and it is conceivable that heating effects and thermal latching are responsible for the steeper transition of the critical current from the first to the second plateau and the lower experimentally measured critical current at the second plateau, in comparison with the calculated $I_c(B)$ that do not include such thermal effects, as shown in figure 6(c).

Nevertheless, the still surprisingly good agreement between theory and experiment may be due to the fact that WSi is a weakly pinning material. Similar superconducting materials with comparable or even weaker bulk pinning are therefore preferable candidates for confirming the theoretical

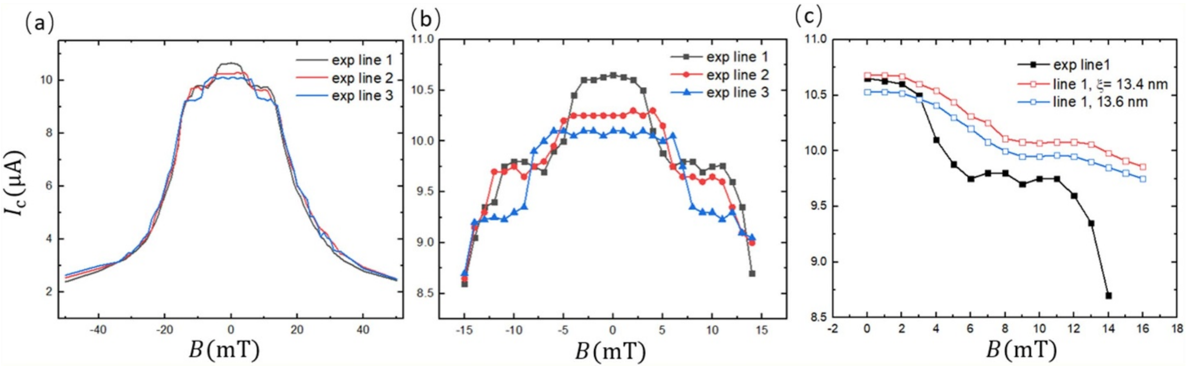

Figure 6. (a) Magnetic field dependence of the critical current I_c: black, red, and blue curves are for exp-lines 1, 2, and 3, respectively; (b) enlarged view of the same for magnetic fields between −15 mT and 15 mT; (c) comparison of the simulated $I_c(B)$ data with the experimental values for exp-line 1.

predictions of vortex dynamics in the absence of bulk pinning. Strong bulk pinning of vortices may effectively modify the properties of superconducting films with an artificial pinhole pattern, making the results of corresponding measurements incomparable to those obtained by theoretical models based on the assumption of zero bulk pinning.

5. Conclusions

In summary, we have studied the vortex dynamics in superconducting microwires with perforated rectangular pinhole structures. The results of simulations based on the time-dependent Ginzburg–Landau equations are compared with corresponding experiments on the magnetic-field dependence of the critical current for three different longitudinal pinhole spacings. The simulations reveal three qualitatively different vortex states, namely a vortex free state at low currents below the critical current, and with increasing current a state with regular vortex flow, followed by a state with a more complex vortex pattern. The occurrence of two distinct plateaus in the field dependence of $I_\mathrm{c}(B)$ contrasts with the observation of a single plateau around $B = 0$ in structures with a single hole or a triangular pinhole arrangement. This field dependence, as well as the qualitative dependence of I_c on the vertical hole spacing, was experimentally confirmed on WSi microwires with identical hole arrangements, thereby confirming the validity and power of the numerical simulations. Certain deviations from the theoretical predictions, such as the observed faster decrease of $I_\mathrm{c}(B)$ with increasing magnetic field beyond the second plateau and the exact location of the second plateau may originate from an oversimplification of the geometrical structure, for example, by implicitly assuming uniform edge pinning along the edges of the microwires and thus neglecting edge roughness and imperfections, or the disregard of a possible thermal latching process.

Despite these shortcomings, our approach may stimulate further related investigations, both theoretically and experimentally, on superconducting microwires containing artificial or natural defects for photon detection applications.

Data availability statement

The data cannot be made publicly available upon publication because no suitable repository exists for hosting data in this field of study. The data that support the findings of this study are available upon reasonable request from the authors.

Acknowledgments

This work was supported by the Swiss National Foundation under Grant No. 20-175554. We thank to Dr. Logan Bishop-Van Horn for fruitful discussions.

ORCID iDs

Dong Zhu 0000-0002-8536-561X
Ilya Charaev 0000-0002-4036-0778
Konstantin Ilin 0009-0000-6828-5530
Andreas Schilling 0000-0002-3898-2498

References

[1] Korneeva Y P, Vodolazov D, Semenov A, Florya I, Simonov N, Baeva E, Korneev A, Goltsman G and Klapwijk T 2018 Optical single-photon detection in micrometer-scale NbN bridges *Phys. Rev. Appl.* **9** 064037

[2] Chiles J, Buckley S M, Lita A, Verma V B, Allmaras J, Korzh B, Shaw M D, Shainline J M, Mirin R P and Nam S W 2020 Superconducting microwire detectors based on WSi with single-photon sensitivity in the near-infrared *Appl. Phys. Lett.* **116** 242602

[3] Charaev I, Morimoto Y, Dane A, Agarwal A, Colangelo M and Berggren K K 2020 Large-area microwire MoSi single-photon detectors at 1550 nm wavelength *Appl. Phys. Lett.* **116** 242603

[4] Li F Y *et al* 2022 Fast and efficient detection of a single photon with hole-patterned superconductor microstrips *Appl. Phys. Lett.* **121** 122601

[5] Zhu D, Charaev I and Schilling A 2023 Effective suppression of dark counts in superconducting microstructures with grid of pinholes in a magnetic field *Supercond. Sci. Technol.* **36** 105012

[6] Ejrnaes M, Cirillo C, Salvoni D, Chianese F, Bruscino C, Ercolano P, Cassinese A, Attanasio C, Pepe G P and

Parlato L 2022 Single photon detection in NbRe superconducting microstrips *Appl. Phys. Lett.* **121** 262601

[7] Xu G-Z *et al* 2021 Superconducting microstrip single-photon detector with system detection efficiency over 90% at 1550 nm *Photon. Res.* **9** 958

[8] Vodolazov D Y 2017 Single-photon detection by a dirty current-carrying superconducting strip based on the kinetic-equation approach *Phys. Rev. Appl.* **7** 034014

[9] Vodolazov D Y 2019 Flux-flow instability in a strongly disordered superconducting strip with an edge barrier for vortex entry *Supercond. Sci. Technol.* **32** 115013

[10] Batson E, Incalza F, Castellani M, Colangelo M, Charaev I, Schilling A, Cherednichenko S and Berggren K K 2024 Effects of helium ion exposure on the single-photon sensitivity of MgB_2 and NbN detectors *IEEE Trans. Appl. Supercond.* **34** 1–6

[11] Charaev I *et al* 2023 Single-photon detection using high-temperature superconductors *Nat. Nanotechnol.* **18** 343

[12] Zhang W, Jia Q, You L, Ou X, Huang H, Zhang L, Li H, Wang Z and Xie X 2019 Saturating intrinsic detection efficiency of superconducting nanowire single-photon detectors via defect engineering *Phys. Rev. Appl.* **12** 044040

[13] Bezuglyj A I, Shklovskij V A, Vovk R V, Bevz V M, Huth M and Dobrovolskiy O V 2019 Local flux-flow instability in superconducting films near T_c *Phys. Rev. B* **99** 174518

[14] Kogan V and Nakagawa N 2021 Moving pearl vortices in thin-film superconductors *Condens. Matter* **6** 4

[15] Vodolazov D Y, Ilin K, Merker M and Siegel M 2016 Defect-controlled vortex generation in current-carrying narrow superconducting strips *Supercond. Sci. Technol.* **29** 025002

[16] Grishakova K S, Degtyarenko P N, Degtyarenko N N, Elesin V F and Kruglov V S 2012 Time dependent Ginzburg-Landau equations for modeling vortices dynamics in type-II superconductors with defects under a transport current *Phys. Proc.* **36** 1206

[17] Horn L B-V 2023 pyTDGL: time-dependent Ginzburg-Landau in Python *Comput. Phys. Commun.* **291** 108799

[18] , Il'in K and Siegel M 2014 Magnetic field stimulated enhancement of the barrier for vortex penetration in bended bridges of thin TaN films *Physica C* **503** 58-61 and the references therein

[19] Ceccarelli L, Vasyukov D, Wyss M, Romagnoli G, Rossi N, Moser L and Poggio M 2019 Imaging pinning and expulsion of individual superconducting vortices in amorphous MoSi thin films *Phys. Rev. B* **100** 104504

[20] Engel A, Renema J J, Il'in K and Semenov A 2015 Detection mechanism of superconducting nanowire single-photon detectors *Supercond. Sci. Technol.* **28** 114003

[21] Ge J-Y, Gladilin V N, Tempere J, Devreese J and Moshchalkov V V 2017 Controlled generation of quantized vortex−antivortex pairs in a superconducting condensate *Nano Lett.* **17** 5003

[22] Sasaki K, Suzuki N and Saito H 2010 Bénard–von Karman vortex street in a Bose-Einstein condensate *Phys. Rev. Lett.* **104** 150404

[23] Wang Y L, Latimer M L, Xiao Z L, Divan R, Ocola L E, Crabtree G W and Kwok W K 2013 Enhancing the critical current of a superconducting film in a wide range of magnetic fields with a conformal array of nanoscale holes *Phys. Rev. B* **87** 22051

[24] Latimer M L, Berdiyorov G R, Xiao Z L, Peeters F M and Kwok W K 2013 Realization of artificial ice systems for magnetic vortices in a superconducting MoGe thin film with patterned nanostructures *Phys. Rev. Lett.* **111** 067001

[25] Latimer M L, Berdiyorov G R, Xiao Z L, Kwok W K and Peeters F M 2012 Vortex interaction enhanced saturation number and caging effect in a superconducting film with a honeycomb array of nanoscale holes *Phys. Rev. B* **85** 012505

[26] Berdiyorov G R, Milosevic M V and Peeters F M 2006 Novel commensurability effects in superconducting films with antidot arrays *Phys. Rev. Lett.* **96** 207001

[27] Berdiyorov G R, Milosevic M V and Peeters F M 2006 Vortex configurations and critical parameters in superconducting thin films containing antidot arrays: nonlinear Ginzburg-Landau theory *Phys. Rev. B* **74** 174512

[28] Li F, Pan X, Chen Q, Yu H, Qiu Y and Zhang L 2025 Characterization of a hole-patterned microstrip superconducting single-photon detector *J. Sel. Top. Quantum Electron.* **31** 3801208